Journal of the Optical Society of America B
OPTICAL PHYSICS

Etchless photonic integrated circuits enabled by bound states in the continuum: tutorial

YUE YU AND XIANKAI SUN*

Department of Electronic Engineering, The Chinese University of Hong Kong, Shatin, New Territories, Hong Kong
**xksun@cuhk.edu.hk*

Received 10 March 2023; revised 5 June 2023; accepted 5 June 2023; posted 6 June 2023; published 10 October 2023

We provide a detailed tutorial demonstrating how the principle of "bound states in the continuum" (BICs) enables ultralow-loss guiding and routing of photons in photonic integrated circuits fabricated with an etchless process. Here, BICs refer to the nondissipative transverse magnetic (TM) polarized bound modes that exist in the transverse electric (TE) polarized continuum. First, we provide a theoretical analysis of BICs based on the coupling between the TM bound modes and the TE continuum, which is next verified by numerically simulated waveguide propagation loss of the TM bound modes for different waveguide geometries. Then, we present the experimental details, which include fabrication processes and characterization methods for various types of BIC-based integrated photonic devices. Finally, we discuss the superiority and versatility of the BIC-based integrated photonic platform, which can be adopted for different thin-film substrates, for different wavelength ranges, and for heterogeneous integration with different functional materials.

https://doi.org/10.1364/JOSAB.489650

1. INTRODUCTION

Bound states in the continuum (BICs) refer to special types of bound states that lie inside a continuous spectrum but still have perfect confinement without any radiation loss. This concept was first proposed by von Neumann and Wigner [1]. Since then, BICs have been widely explored in optical [2–7], acoustic [8–11], and mechanical [12–16] domains to reduce dissipation loss, which enabled many unprecedented applications. The interest in photonic BICs has grown markedly in recent years due to the advancement in micro/nanofabrication technologies. To date, photonic BICs have been observed in various structures: Plotnik *et al.* first observed photonic BICs in an optical waveguide array in 2011 [17]; Hsu *et al.* experimentally demonstrated BICs in a photonic crystal slab in 2013 [18]; Kodigala *et al.* reported BIC lasing action from an active photonic crystal slab in 2017 [19]; Koshelev *et al.* revealed BICs with high-Q resonances in asymmetric metasurfaces in 2018 [20]; Rybin *et al.* revealed quasi-BICs in subwavelength dielectric resonators in 2017 [7], which were adopted for enhancing nonlinear effects and for increasing second-harmonic generation efficiency by Koshelev *et al.* in 2020 [21]. This tutorial focuses on BICs in optical waveguides for building low-loss photonic integrated circuits (PICs). A similar idea dates back to 1978 when Peng and Oliner theoretically predicted leakage cancellation and sharp resonances in open dielectric waveguides [22]. Later, Peng *et al.* and Ogusu performed detailed analyses of such waveguides with mathematical formulations based on a mode-coupling technique [23,24]. It was revealed that these phenomena were caused by TE–TM mode coupling at strip boundaries, and cancellation could occur at suitable strip widths. This width-dependent lateral leakage loss behavior was further verified in ridge waveguides, couplers, and disk and ring resonators on silicon-on-insulator platforms [25–28] and was later recognized as a type of BIC [29]. Recently, similar phenomena were studied in a new architecture, where the high-refractive-index ridge waveguide was replaced with a low-refractive-index waveguide on a high-refractive-index thin film. Zou *et al.* theoretically proposed such BICs in optical waveguides and microresonators in 2015 [3], which were experimentally realized for constructing ultralow-loss PICs by Yu *et al.* [4]. This configuration of photonic BICs breaks the refractive index limitation of conventional photonic architectures and has since enabled a new class of integrated photonic devices [30–48] that can be fabricated with an etchless process. This method can be adopted generically for constructing PICs in other functional materials, which holds great promise in the development of classical and quantum photonics. Without doubt, the vigorous development of photonic BICs has offered inspiration to other areas and will continue enabling multidisciplinary applications.

This tutorial focuses on BIC-enabled ultralow-loss guiding and routing of photons in low-refractive-index PICs on a high-refractive-index substrate, and provides a detailed theoretical analysis, numerical simulation, and fabrication processes of such PICs. It is targeted at researchers with basic knowledge of physics, numerical modeling, and micro/nanofabrication who desire to design and fabricate their own PICs and devices under the principle of BICs. This paper is structured as follows: In

Section 2, we analyze the photonic potential well and propagation loss of BIC modes. In Section 3, we build physical models in COMSOL Multiphysics and simulate the effective refractive index for obtaining the numerically calculated waveguide propagation loss and cavity Q factor. In Section 4, we present the fabrication processes for BIC-based PICs and devices. In Section 5, we provide characterization methods for experimentally verifying BICs in waveguides and microcavities. In Section 6, we discuss the superiority of the BIC-based photonic platform for modern PICs.

2. THEORETICAL ANALYSIS OF BICS IN ETCHLESS PICS

BIC-based PICs are constructed by patterning a low-refractive-index material on top of a high-refractive-index thin-film substrate without the need for etching the high-refractive-index thin film. The high-refractive-index thin film can be any optically transparent material. Here, without loss of generality, we use a lithium-niobate-on-insulator (LNOI) substrate as an example, as shown in Fig. 1. To achieve ultralow-loss guiding and routing of light in such PICs, one needs to understand the physical mechanism of lateral confinement of a propagating bound mode. In this section, we theoretically analyze the dissipation mechanism in photonic waveguides and microresonators and derive the conditions for realizing BICs in each scenario.

A. Waveguides

BIC waveguides are constructed by patterning a layer of polymer on a z-cut LNOI substrate. The LNOI substrate is composed of a lithium niobate (LN) thin film with 150 or 300 nm thickness on a 2-μm-thick silica layer on silicon for PICs operating at near-visible or telecom wavelengths, respectively. Note that the analysis in this part applies only to straight waveguides, while the dissipation mechanism in a bent waveguide is essentially the same as that in a microring cavity, which will be addressed in Section 2.B. By using the effective-medium method [8], we divide the cross-sectional structure into three parts (I, II, III), as shown in Fig. 2(a). Then, we calculate the effective refractive index of the slab waveguide in each part (assuming the same layer composition extends infinitely in the x direction). Note that in part I and part III, the slab waveguide structures are the same and thus possess the same light propagation properties. Figure 2(b) shows the effective refractive index distributions for TE and TM polarizations in the three parts. It is clear that the patterned overlay polymer waveguide in part II induces a higher effective refractive index in the same region. Because the potential for photons is determined by the negative of the refractive index, a region with a higher refractive index provides a lower potential for photons where a bound mode can be supported. It is worth clarifying that although both TE- and TM-polarized bound modes can be supported in their respective potential well, they have different features and thus should be used for different applications [49].

First, it is clear from Fig. 2(b) that the difference between the effective refractive indices inside and outside the waveguide Δn_{eff} $(= n_{\mathrm{eff}}^{(\mathrm{II})} - n_{\mathrm{eff}}^{(\mathrm{I,III})})$ is different for TE and TM polarizations. Δn_{eff} for TM polarization is much larger than that for TE polarization, so the potential well for the TM polarization is much deeper than that for the TE polarization. Therefore, TM-polarized bound modes (subject to the BIC condition discussed below) achieve a tighter lateral confinement than TE-polarized bound modes. For this reason, TM-polarized modes are preferred in PICs that include bent waveguides and/or microcavities for achieving lower loss or higher integration density [3,4].

Second, the potential well for TE-polarized photons supports regular TE bound modes, but the scenario becomes more interesting for TM-polarized bound modes. Because the effective refractive indices for TE polarization in part I and part III are higher than that for TM polarization in part II, the TM bound mode is actually located inside the continuous spectrum of the TE-polarized modes. Usually, there is coupling between the TM bound mode and the TE continuous modes, and their coupling can be formulated with the following Hamiltonian:

$$H = \hbar\beta_b b^\dagger b + \hbar \sum_m \beta_m c_m^\dagger c_m + \hbar \sum_m g_m (c_m^\dagger b + c_m b^\dagger). \quad (1)$$

Here, b and c_m are the annihilation operators of the TM bound mode and the mth TE continuous mode, respectively, and β_b

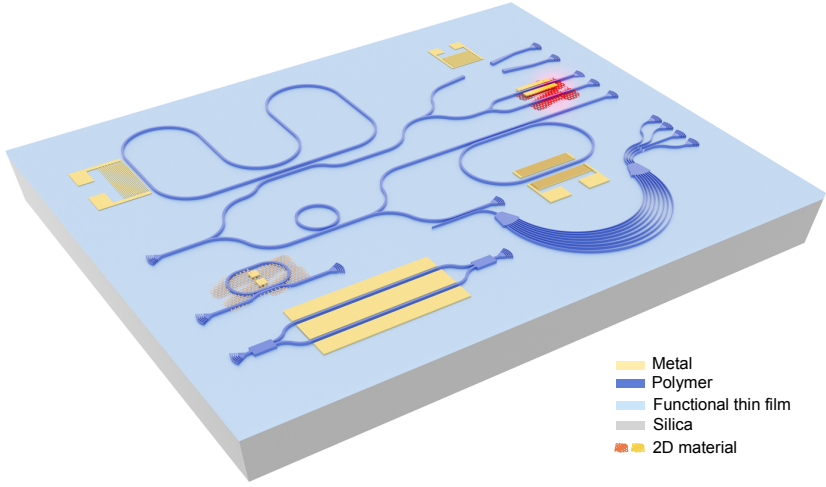

Fig. 1. Schematic illustration of a BIC-enabled photonic integrated circuit fabricated with an etchless process.

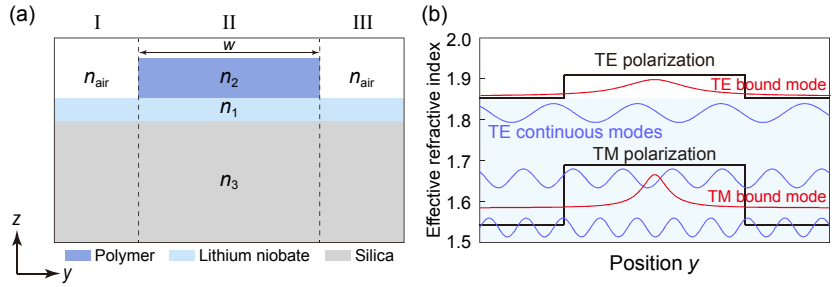

Fig. 2. (a) Cross section of the hybrid waveguide structure that can support a BIC. (b) Effective refractive index distributions for TE and TM polarizations in the waveguide structure in (a).

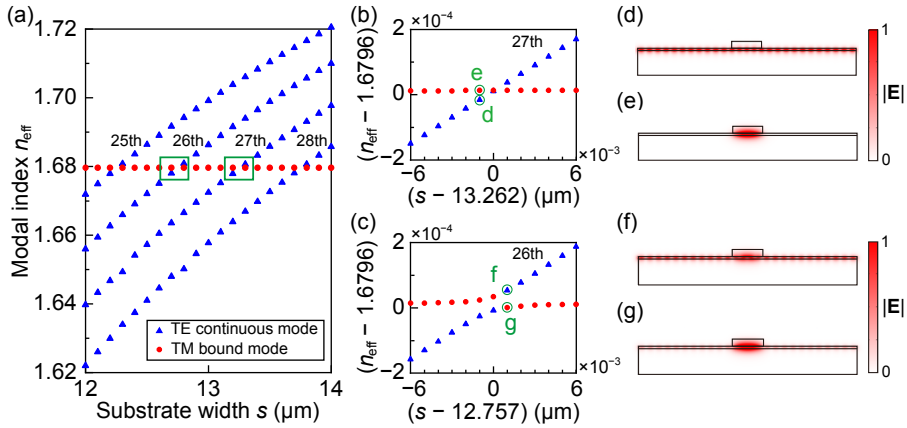

Fig. 3. (a) Modal indices of TE continuous modes (blue triangles) and fundamental TM bound mode (red dots). (b) Close-up of the crossing between the 27th TE continuous mode and the fundamental TM bound mode. (c) Close-up of the anticrossing between the 26th TE continuous mode and the fundamental TM bound mode. (d)–(g) Normalized modal field profiles (|**E**| component) at the respective marked points in (b) and (c).

and β_m are the corresponding propagation constants. g_m is the strength of coupling between the TM bound mode and the mth TE continuous mode. In a structure where the substrate has a finite width s, the TE continuous modes are actually discretized under the quantization condition $k_y s = 2\pi m$, where k_y is the wave vector along the y direction [Fig. 3(a)]. Figures 3(b) and 3(c) plot close-ups of the modal indices n_{eff} near the crossing and anticrossing points marked in Fig. 3(a). Figures 3(d)–3(g) show the modal field profiles (|**E**|) at the respective marked points in Figs. 3(b) and 3(c). The TM bound mode contains an E_y component, with odd parity, scattering at the two edges of the waveguide. Therefore, for odd m, the mth TE continuous mode has even parity in E_y and thus is orthogonal to the TM bound mode causing no modal coupling. For even m, the mth TE continuous mode has odd parity in E_y and thus has nonzero overlap with the TM bound mode causing modal coupling. The coupling strength g_m is determined by the normalized field overlap between the TM bound mode and the mth TE continuous mode.

Due to scattering, the TM bound mode interacts with the TE continuous modes at the two edges of the waveguide. Therefore, the TM bound mode has two channels of dissipation into each TE continuous mode. In a straight waveguide, the rates of dissipation are equal through the two channels, and thus the total effective coupling strength is expressed as

$$g_m \approx \tilde{g}_m \frac{\left|1 - e^{ik_y w}\right|}{2w\sqrt{s}}, \tag{2}$$

where $k_y w \approx k_0 w \sqrt{n_{\text{II,TE}}^2 - n_m^2}$ is the phase difference between the two interfering dissipation channels, and $\tilde{g}_m$ is a constant that can be obtained from numerical simulation. Equation (2) unveils the physical mechanism for eliminating the loss of a bound mode to the continuum: *constructing multiple loss channels and controlling their phase difference to realize destructive interference between them*. In a real structure, the substrate has an infinitely large width ($s \to \infty$), and thus the coupling between the TM bound mode and the TE continuous modes leads to the Markov system–environment interaction [50]. The optical power of the TM bound mode decays exponentially during its propagation along the x direction: $P(x) = P(0)\mathrm{e}^{-x/L}$, with L being the decay length expressed as

$$L \approx \frac{w^2}{\tilde{g}_m^2 \sin^2(k_y w/2)} \frac{\sqrt{n_{\text{II,TE}}^2 - n_b^2}}{2n_b}. \tag{3}$$

Here, n_b is the modal index of the TM bound mode, which is close to n_m at the anticrossing region. It turns out that L does not depend on the substrate width s, and thus the properties of the TM bound mode for structures with a finite s should also apply to those with an infinite s. According to Eq. (3), the TM bound mode's decay length L can reach infinity at certain waveguide widths w that satisfy the condition of $\sin(k_y w/2) = 0$. Under this condition, the TM bound mode has no energy dissipation into the TE continuum and thus becomes a theoretically lossless BIC.

B. Microcavities

Similar to the straight waveguide discussed in Section 2.A, in a microring cavity (formed by a closed-loop bent waveguide), the TM bound mode of the bent waveguide is usually coupled with the waveguide's TE continuous modes, causing energy dissipation of the former into the latter. Different from the case of a straight waveguide, the TM bound mode in a bent waveguide is distributed asymmetrically with a slight shift to the outer waveguide edge. Consequently, the TM bound mode has unequal rates of dissipation through the two channels. The loss of the TM bound mode to the TE continuum can be estimated from $|J_q(n_b k_r r_b) - \xi J_q(n_b k_r (r_b - w_b)|$ [51–53], where J_q is the qth-order Bessel function, k_r is the wave vector along the radial direction, r_b is the bend radius of the outer waveguide edge, w_b is the waveguide width, and ξ is the ratio of electric field amplitudes of the TM bound mode at the inner and outer waveguide edges. A microdisk cavity with a radius of r_d can be treated as a special case of the microring cavity where the waveguide width is equal to the bend radius of the outer waveguide edge. In this connection, the loss of the TM bound mode to the TE continuum in a microdisk cavity can be estimated from $|J_q(n_b k_r r_d)|$. As r_b (r_d) or w_b varies, the loss of the TM bound mode in both types of microcavities exhibits oscillatory behavior. When the loss reaches zero, the TM bound mode has no energy dissipation into the TE continuum and thus becomes a theoretically lossless BIC. For microcavities, the Q factor is usually used for quantifying a cavity's capability of storing energy. Since the Q factor is inversely proportional to the propagation loss of the circulating mode, the Q factor of these microcavities also shows oscillation and can reach infinity at certain combinations of geometric parameters.

3. NUMERICAL CALCULATION OF PROPAGATION LOSS AND Q FACTOR

We use commercial software COMSOL Multiphysics 5.5 to obtain the complex modal index in different structures, based on which we can obtain the numerically calculated propagation loss for waveguides and Q factors for microcavities. The detailed simulation processes can be found in Supplement 1.

For a straight waveguide, the propagation loss of the TM bound mode in units of dB/cm is calculated from $20 \log_{10}\{\exp$

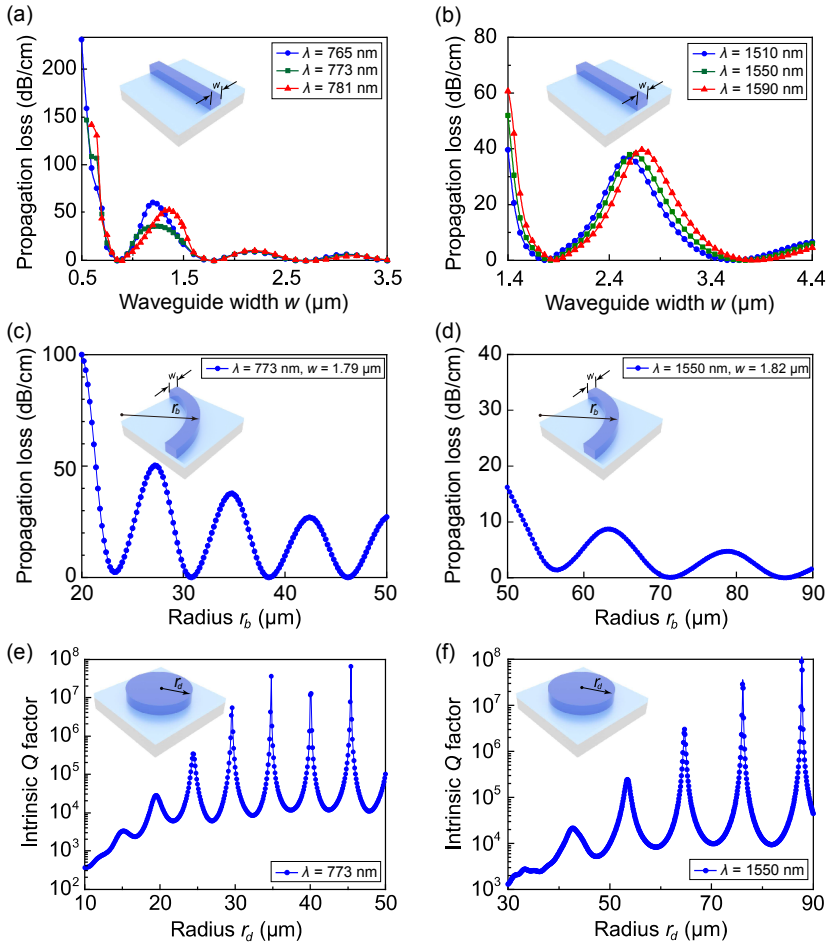

Fig. 4. (a) Simulated propagation loss of the straight waveguide as a function of the waveguide width w at wavelengths of 765, 773, and 781 nm. (b) Simulated propagation loss of the straight waveguide as a function of the waveguide width w at wavelengths of 1510, 1550, and 1590 nm. (c), (d) Simulated propagation loss of the bent waveguide as a function of the bend radius r_b at wavelengths of 773 nm (c) and 1550 nm (d) with waveguide width w fixed at 1.79 μm (c) and 1.82 μm (d). (e), (f) Simulated intrinsic Q factor of the microdisk as a function of the disk radius r_d at wavelengths of 773 nm (e) and 1550 nm (f).

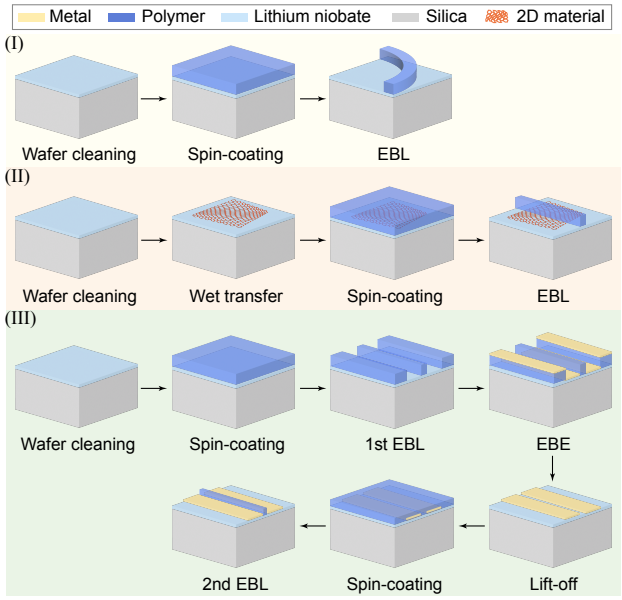

Fig. 5. Procedures for fabricating different types of component devices in BIC-enabled etchless photonic integrated circuits: (I) passive optical devices, (II) 2D-material-integrated devices, and (III) electro-optic and acousto-optic devices. EBL, electron-beam lithography; EBE, electron-beam evaporation.

$[2\pi \cdot \mathrm{imag}(n) \times 1\ \mathrm{cm}/\lambda]\}$. Figures 4(a) and 4(b) plot the calculated propagation loss of the fundamental TM bound mode in a straight waveguide as a function of the waveguide width w at near-visible and telecom wavelengths, respectively. The propagation loss in both wavelength bands shows oscillation and approaches zero at certain w values, which is consistent with the theoretical results in Section 2.A. At those waveguide widths, the TM bound mode is totally decoupled from the TE continuum and becomes a theoretically lossless BIC. For a bent waveguide, the propagation loss of the TM bound mode in units of dB/cm is calculated from $20\log_{10}\{\exp[2\pi \cdot \mathrm{imag}(n_b) \times 1\ \mathrm{cm} \times 1\ \mathrm{m}/\lambda \cdot r_b]\}$. Figures 4(c) and 4(d) plot the calculated propagation loss of the fundamental TM bound mode in a bent waveguide as a function of the bend radius r_b at near-visible and telecom wavelengths, respectively. For microdisk cavities, the intrinsic Q factor is calculated from $\mathrm{real}(n_d)/[2 \cdot \mathrm{imag}(n_d)]$. Figures 4(e) and 4(f) plot the calculated intrinsic Q factor of the microdisk as a function of the disk radius r_d at wavelengths of 773 and 1550 nm, respectively. The intrinsic Q factor at both wavelengths shows oscillation and approaches infinity at certain r_d values, which is consistent with the theoretical results in Section 2.B.

4. FABRICATION OF COMPONENT DEVICES IN ETCHLESS PICS

Figure 5 shows the procedures for fabricating different types of component devices in BIC-enabled etchless PICs.

The procedure (I) for fabricating passive optical devices on an etchless LNOI platform includes only one step of electron-beam lithography (EBL). After wafer cleaning with acetone and isopropanol, a polymer (ZEP520A) is spin-coated on the wafer at 2300–3300 rpm for 1 min and then prebaked on a hot plate at 180°C for 3 min, which produces a polymer thin film with 500–400 nm thickness. Then, the device patterns are defined in the polymer thin film by using a high-resolution EBL system (Elionix ELS7800) with a beam current of 500 pA and a dose of 180−220 $\mu C/cm^2$. After the electron-beam exposure, the wafer is developed in a developer ZED-N50 at 0°C for 1 min, then rinsed in a mixture of methyl isobutyl ketone and isopropanol (9:1) at room temperature for 30 s, and blow-dried.

The procedure (II) for fabricating 2D-material-integrated devices on an etchless LNOI platform is similar to procedure (I). After wafer cleaning with acetone and isopropanol, the 2D material is wet transferred onto the wafer, which is then prebaked on a hot plate at 120°C for 30 min. After transferring the 2D material, the rest of the processes follow those in procedure (I).

The procedure (III) for fabricating electro-optic and acousto-optic devices on an etchless LNOI platform requires an additional step of EBL and metal deposition for fabricating electrodes before patterning the photonic structures. The process parameters for the two EBL steps are the same as those in procedure (I). After the first EBL step, stacked layers of 5-nm-thick titanium and 80-nm-thick gold are deposited on the wafer by using electron-beam evaporation (EBE). Then, the electrodes are fabricated by a lift-off process, which involves soaking of the wafer in dimethyl sulfoxide at 120°C for 30 min. After fabricating the electrodes, the rest of the processes follow those in procedure (I).

The fabricated devices are quite stable in the ambient environment. They do not have noticeable degradation in their performance after storage in a dry box for several years.

5. EXPERIMENTAL VERIFICATION OF BICS IN ETCHLESS PICS

We experimentally verify the BICs by characterizing the component devices in the PICs fabricated on the etchless LNOI platform.

A. Waveguides

To verify the BICs in waveguides, we need to measure the propagation loss of the waveguides with different widths. In a practical experimental setup, there is insertion loss when coupling light between optical fibers and on-chip waveguides. The total loss in the fiber-to-fiber transmission measurement includes both the propagation loss in the on-chip waveguide and insertion loss during fiber-to-chip coupling. To exclude the effect of insertion loss, we fabricate waveguides with the same width but different lengths (say, L_1 and L_2) on the same chip and obtain the fiber-to-fiber transmissions of these devices (say, T_1 and T_2) in units of dB. Then, we obtain the propagation loss of the waveguides at this width from $(T_2 - T_1)/(L_1 - L_2)$. The experimental results agreed excellently with the simulated results, and we measured minimal propagation losses of 1.8 and 1.5 dB/cm from waveguides operating at wavelengths of 773 and 1550 nm, respectively [4,44].

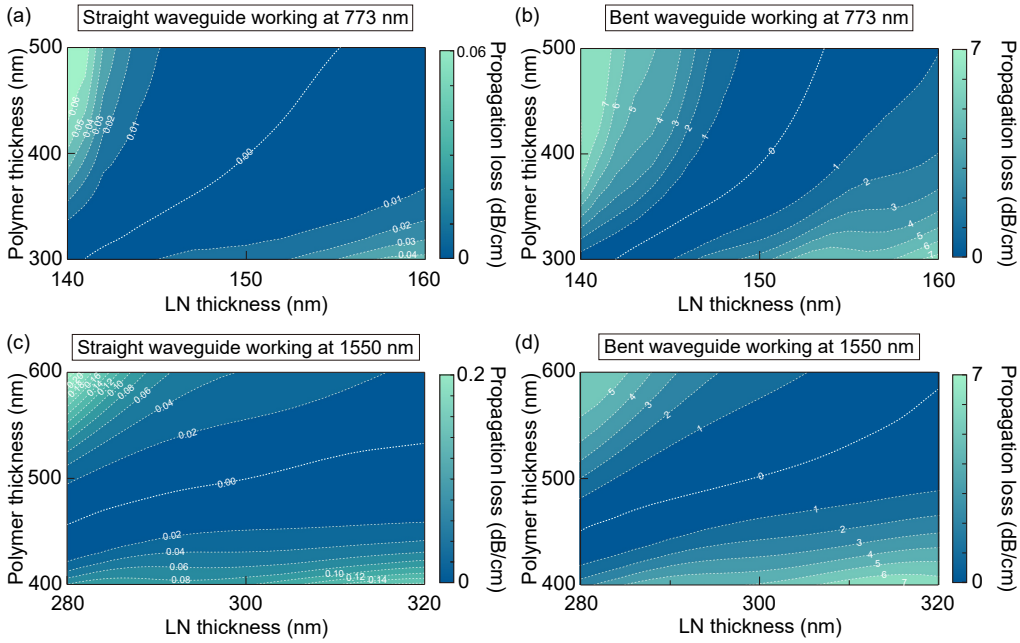

Fig. 6. (a), (b) Simulated propagation loss of the TM_0 mode as a function of the polymer and LN thicknesses at the wavelength of 773 nm in straight (a) and bent (b) waveguides. The waveguide width for the straight waveguide is fixed at 1.79 μm. The waveguide width and bend radius for the bent waveguide are fixed at 1.79 and 69.7 μm, respectively. (c), (d) Simulated propagation loss of the TM_0 mode as a function of the polymer and LN thicknesses at the wavelength of 1550 nm in straight (c) and bent (d) waveguides. The waveguide width for the straight waveguide is fixed at 1.82 μm. The waveguide width and bend radius for the bent waveguide are fixed at 1.82 and 71.4 μm, respectively.

B. Microcavities

To verify the BICs in microcavities, we need to fabricate many microring and microdisk cavities with different radii on the same chip. We also fabricate bus waveguides on the chip in close proximity to these microcavities to access the circulating modes in them. Then, we measure the transmission spectra from the bus waveguides and obtain the loaded cavity Q factors Q_l by using Lorentzian fitting to the individual cavity resonances. The intrinsic quality factors Q_i can be determined based on the waveguide–cavity coupling condition. Under the critical coupling condition, we have $Q_i = 2Q_l$. Under the under-coupling or over-coupling condition, we have $Q_i = 2Q_l/(1+\sqrt{T})$ or $Q_i = 2Q_l/(1-\sqrt{T})$, respectively, where T is the normalized transmission at the cavity resonance. The experimental results agreed excellently with the simulated results, and we measured maximal intrinsic Q factors of 1.1×10^6 and 5.8×10^5 from microcavities operating at wavelengths of 773 and 1550 nm, respectively [4,44].

C. Robustness Analysis

These BIC-based PICs have excellent robustness against structural variation. Figure 6 shows the calculated propagation loss of the fundamental TM mode as the polymer and LN layer thicknesses deviate slightly from the designed BIC point, where the targeted geometric parameters are $(h_{LN}, h_{ZEP}, w, r_b) = (300\ \text{nm}, 500\ \text{nm}, 1.82\ \mu\text{m}, 71.4\ \mu\text{m})$ for operation at the wavelength of 1550 nm and $(h_{LN}, h_{ZEP}, w, r_b) = (150\ \text{nm}, 400\ \text{nm}, 1.79\ \mu\text{m}, 69.7\ \mu\text{m})$ for operation at the wavelength of 773 nm. The simulated results show that for straight waveguides, variations in the polymer and LN layer thicknesses have little effect on the propagation loss of the BIC mode, while bent waveguides are more sensitive to variations in the polymer and LN layer thicknesses. With continuous improvement in wafer processing technologies, nowadays the variations in the polymer and LN layer thicknesses across a single chip can be negligible. Given a set of polymer and LN layer thicknesses not far away from their designed values, we can always tweak the other geometric parameters to achieve the BIC.

The excellent robustness provides the foundation for practical applications of BIC-based PICs. Based on the elementary structures of waveguides and microcavities, we can realize many types of functional photonic devices on an etchless integrated platform, such as multimode directional couplers, power splitters, Mach–Zehnder interferometers, arrayed waveguide gratings [4,44,47], etc. By harnessing the excellent nonlinear properties of LN, we can also explore high-efficiency electro-optic modulation, acousto-optic modulation, and frequency conversion on an etchless LNOI platform [43,45,46].

6. DISCUSSION AND CONCLUSION

Overcoming the challenges in etching single-crystal materials during micro- and nanofabrication, BIC-based PICs serve as a new paradigm for integrated photonics. Apart from the examples in this tutorial, the BIC-based integrated photonic platform can be adopted for different thin-film substrates, for different wavelength ranges, and for heterogeneous integration with different functional materials. For example, when integrated with optically active materials such as perovskites, 2D transition metal dichalcogenides, or quantum-dot-doped polymers, this platform can provide a low-cost yet reliable solution to on-chip

single-photon sources, optical amplifiers, and low-threshold lasers. Therefore, it is expected that the BIC-based integrated photonic platform will facilitate the development of both passive and active PICs in all thin-film optical materials operating in all wavelength ranges, which will enable unprecedented applications in optical communication, imaging, sensing, and information processing.

In this tutorial, we have analyzed the dissipation mechanism in a hybrid photonic architecture, which is formed by patterning a low-refractive-index material on a high-refractive-index thin-film substrate and thus may avoid etching in its fabrication. We theoretically derived the conditions for obtaining BICs in waveguides and microcavities based on the hybrid photonic architecture, which are the building blocks of an etchless PIC. Then, we provided the detailed methods for numerically calculating the waveguide propagation loss and cavity Q factor in these structures. After that, we provided the detailed procedures for fabricating different types of component devices in BIC-enabled etchless PICs. Finally, we provided the detailed methods for measuring the fabricated devices and experimentally verifying the BICs.

This tutorial serves as a starting point for those who want to develop their own research directions and applications of BIC-based etchless PICs. While this tutorial focuses only on the elementary components in a PIC and takes the LNOI platform as an example, the fundamental principles can be adopted for building etchless integrated photonic platforms based on other thin-film materials. Therefore, we encourage readers to leverage the interesting yet convenient technology for discovering new physics or developing new engineering applications in related areas.

Funding. Research Grants Council of Hong Kong (14206318, C4050-21E); The Chinese University of Hong Kong (Group Research Scheme).

Acknowledgment. The authors thank Prof. Zejie Yu at Zhejiang University for helpful discussions.

Disclosures. The authors declare no conflicts of interest.

Data availability. Data underlying the results presented in this paper are not publicly available at this time but may be obtained from the authors upon reasonable request.

Supplemental document. See Supplement 1 for supporting content.

REFERENCES

1. J. von Neumann and E. Wigner, "On some peculiar discrete eigenvalues," Phys. Z **30**, 465–467 (1929).
2. D. Marinica, A. Borisov, and S. Shabanov, "Bound states in the continuum in photonics," Phys. Rev. Lett. **100**, 183902 (2008).
3. C. L. Zou, J. M. Cui, F. W. Sun, X. Xiong, X. B. Zou, Z. F. Han, and G. C. Guo, "Guiding light through optical bound states in the continuum for ultrahigh-Q microresonators," Laser Photon. Rev. **9**, 114–119 (2015).
4. Z. Yu, X. Xi, J. Ma, H. K. Tsang, C.-L. Zou, and X. Sun, "Photonic integrated circuits with bound states in the continuum," Optica **6**, 1342–1348 (2019).
5. E. N. Bulgakov and A. F. Sadreev, "Bound states in the continuum in photonic waveguides inspired by defects," Phys. Rev. B **78**, 075105 (2008).
6. R. Kikkawa, M. Nishida, and Y. Kadoya, "Polarization-based branch selection of bound states in the continuum in dielectric waveguide modes anti-crossed by a metal grating," New J. Phys. **21**, 113020 (2019).
7. M. V. Rybin, K. L. Koshelev, Z. F. Sadrieva, K. B. Samusev, A. A. Bogdanov, M. F. Limonov, and Y. S. Kivshar, "High-Q supercavity modes in subwavelength dielectric resonators," Phys. Rev. Lett. **119**, 243901 (2017).
8. R. Parker, "Resonance effects in wake shedding from parallel plates: some experimental observations," J. Sound Vibr. **4**, 62–72 (1966).
9. A. F. Sadreev, "Interference traps waves in an open system: bound states in the continuum," Rep. Prog. Phys. **84**, 055901 (2021).
10. I. Deriy, I. Toftul, M. Petrov, and A. Bogdanov, "Bound states in the continuum in compact acoustic resonators," Phys. Rev. Lett. **128**, 084301 (2022).
11. A. Lyapina, D. Maksimov, A. Pilipchuk, and A. Sadreev, "Bound states in the continuum in open acoustic resonators," J. Fluid Mech. **780**, 370–387 (2015).
12. Y. Chen, Z. Shen, X. Xiong, C.-H. Dong, C.-L. Zou, and G.-C. Guo, "Mechanical bound state in the continuum for optomechanical microresonators," New J. Phys. **18**, 063031 (2016).
13. M. Zhao and K. Fang, "Mechanical bound states in the continuum for macroscopic optomechanics," Opt. Express **27**, 10138–10151 (2019).
14. H. Tong, S. Liu, M. Zhao, and K. Fang, "Observation of phonon trapping in the continuum with topological charges," Nat. Commun. **11**, 5216 (2020).
15. S. Liu, H. Tong, and K. Fang, "Optomechanical crystal with bound states in the continuum," Nat. Commun. **13**, 3187 (2022).
16. Y. Yu, X. Xi, and X. Sun, "Observation of mechanical bound states in the continuum in an optomechanical microresonator," Light Sci. Appl. **11**, 328 (2022).
17. Y. Plotnik, O. Peleg, F. Dreisow, M. Heinrich, S. Nolte, A. Szameit, and M. Segev, "Experimental observation of optical bound states in the continuum," Phys. Rev. Lett. **107**, 183901 (2011).
18. C. W. Hsu, B. Zhen, J. Lee, S.-L. Chua, S. G. Johnson, J. D. Joannopoulos, and M. Soljačić, "Observation of trapped light within the radiation continuum," Nature **499**, 188–191 (2013).
19. A. Kodigala, T. Lepetit, Q. Gu, B. Bahari, Y. Fainman, and B. Kanté, "Lasing action from photonic bound states in continuum," Nature **541**, 196–199 (2017).
20. K. Koshelev, S. Lepeshov, M. Liu, A. Bogdanov, and Y. Kivshar, "Asymmetric metasurfaces with high-Q resonances governed by bound states in the continuum," Phys. Rev. Lett. **121**, 193903 (2018).
21. K. Koshelev, S. Kruk, E. Melik-Gaykazyan, J.-H. Choi, A. Bogdanov, H.-G. Park, and Y. Kivshar, "Subwavelength dielectric resonators for nonlinear nanophotonics," Science **367**, 288–292 (2020).
22. S.-T. Peng and A. A. Oliner, "Leakage and resonance effects on strip waveguides for integrated optics," IEICE Trans. **61**, 151–153 (1978).
23. S.-T. Peng and A. A. Oliner, "Guidance and leakage properties of a class of open dielectric waveguides: Part I-Mathematical formulations," IEEE Trans. Microw. Theory Tech. **29**, 843–855 (1981).
24. K. Ogusu, "Optical strip waveguide: a detailed analysis including leaky modes," J. Opt. Soc. Am. **73**, 353–357 (1983).
25. M. Webster, R. Pafchek, A. Mitchell, and T. Koch, "Width dependence of inherent TM-mode lateral leakage loss in silicon-on-insulator ridge waveguides," IEEE Photon. Technol. Lett. **19**, 429–431 (2007).
26. T. G. Nguyen, R. S. Tummidi, T. L. Koch, and A. Mitchell, "Rigorous modeling of lateral leakage loss in SOI thin-ridge waveguides and couplers," IEEE Photon. Technol. Lett. **21**, 486–488 (2009).
27. T. G. Nguyen, R. S. Tummidi, T. L. Koch, and A. Mitchell, "Lateral leakage of TM-like mode in thin-ridge silicon-on-insulator bent waveguides and ring resonators," Opt. Express **18**, 7243–7252 (2010).
28. T. G. Nguyen, R. S. Tummidi, T. L. Koch, and A. Mitchell, "Lateral leakage in TM-like whispering gallery mode of thin-ridge silicon-on-insulator disk resonators," Opt. Lett. **34**, 980–982 (2009).
29. T. G. Nguyen, A. Boes, and A. Mitchell, "Lateral leakage in silicon photonics: theory, applications, and future directions," IEEE J. Sel. Top. Quantum Electron. **26**, 8805388 (2020).
30. X. Xu and S. Jin, "Strong coupling of single quantum dots with low-refractive-index/high-refractive-index materials at room temperature," Sci. Adv. **6**, eabb3095 (2020).
31. H. Tang, Y. Wang, Y. Chen, K. Wang, X. He, C. Huang, S. Xiao, S. Yu, and Q. Song, "Ultrahigh-Q lead halide perovskite microlasers," Nano Lett. **23**, 3418–3425 (2023).

32. Z. Gu, S. Jiang, C. Liu, and N. Zhang, "Robust bound states in the continuum in a dual waveguide system," Photon. Res. **11**, 575–580 (2023).
33. X. Xu, T. Inaba, T. Tsuchizawa, A. Ishizawa, H. Sanada, T. Tawara, H. Omi, K. Oguri, and H. Gotoh, "Low-loss erbium-incorporated rare-earth oxide waveguides on Si with bound states in the continuum and the large optical signal enhancement in them," Opt. Express **29**, 41132–41143 (2021).
34. Z. Zhen, S.-Y. Jin, R. Jie, H.-Y. Liang, and X.-S. Xu, "Strong coupling between colloidal quantum dots and a microcavity with hybrid structure at room temperature," Photon. Res. **10**, 913–921 (2022).
35. G. Y. Chen, Z. X. Li, Y. H. Chen, and X. D. Zhang, "Highly efficient polarization-entangled photon-pair generation in lithium niobate waveguides based on bound states in continuum," Opt. Express **29**, 12110–12123 (2021).
36. X.-J. Liu, Y. Yu, D. Liu, Q.-L. Cui, X. Qi, Y. Chen, G. Qu, L. Song, G.-P. Guo, G.-C. Guo, X. Sun, and X.-F. Ren, "Coupling of photon emitters in monolayer WS_2 with a photonic waveguide based on bound states in the continuum," Nano Lett. **23**, 3209–3216 (2023).
37. H. Qin, X. Shi, and H. Ou, "Exceptional points at bound states in the continuum in photonic integrated circuits," Nanophotonics **11**, 4909–4917 (2022).
38. J. Zhang, B. Pan, W. Liu, D. Dai, and Y. Shi, "Ultra-compact electro-optic modulator based on etchless lithium niobate photonic crystal nanobeam cavity," Opt. Express **30**, 20839–20846 (2022).
39. X. Li, J. Ma, S. Liu, P. Huang, B. Chen, D. Wei, and J. Liu, "Efficient second harmonic generation by harnessing bound states in the continuum in semi-nonlinear etchless lithium niobate waveguides," Light Sci. Appl. **11**, 317 (2022).
40. Z. Yu, Y. Wang, B. Sun, Y. Tong, J. B. Xu, H. K. Tsang, and X. Sun, "Hybrid 2D-material photonics with bound states in the continuum," Adv. Opt. Mater. **7**, 1901306 (2019).
41. Z. Yu, Y. Tong, H. K. Tsang, and X. Sun, "High-dimensional communication on etchless lithium niobate platform with photonic bound states in the continuum," Nat. Commun. **11**, 2602 (2020).
42. Y. Wang, Z. Yu, Z. Zhang, B. Sun, Y. Tong, J.-B. Xu, X. Sun, and H. K. Tsang, "Bound-states-in-continuum hybrid integration of 2D platinum diselenide on silicon nitride for high-speed photodetectors," ACS Photon. **7**, 2643–2649 (2020).
43. Z. Yu and X. Sun, "Gigahertz acousto-optic modulation and frequency shifting on etchless lithium niobate integrated platform," ACS Photon. **8**, 798–803 (2021).
44. Y. Yu, Z. Yu, L. Wang, and X. Sun, "Ultralow-loss etchless lithium niobate integrated photonics at near-visible wavelengths," Adv. Opt. Mater. **9**, 2100060 (2021).
45. Y. Yu, L. Wang, and X. Sun, "Demonstration of on-chip gigahertz acousto-optic modulation at near-visible wavelengths," Nanophotonics **10**, 4323–4329 (2021).
46. F. Ye, Y. Yu, X. Xi, and X. Sun, "Second-harmonic generation in etchless lithium niobate nanophotonic waveguides with bound states in the continuum," Laser Photon. Rev. **16**, 2100429 (2022).
47. Y. Yu, Z. Yu, Z. Zhang, H. K. Tsang, and X. Sun, "Wavelength-division multiplexing on an etchless lithium niobate integrated platform," ACS Photon. **9**, 3253–3259 (2022).
48. Z. Yu and X. Sun, "Acousto-optic modulation of photonic bound state in the continuum," Light Sci. Appl. **9**, 1 (2020).
49. J. Čtyroký, J. Petráček, V. Kuzmiak, and I. Richter, "Bound modes in the continuum in integrated photonic $LiNbO_3$ waveguides: are they always beneficial?" Opt. Express **31**, 44–55 (2023).
50. C.-L. Zou, X.-D. Chen, X. Xiong, F.-W. Sun, X.-B. Zou, Z.-F. Han, and G.-C. Guo, "Photonic simulation of system-environment interaction: non-Markovian processes and dynamical decoupling," Phys. Rev. A **88**, 063806 (2013).
51. M. Oxborrow, "Traceable 2-D finite-element simulation of the whispering-gallery modes of axisymmetric electromagnetic resonators," IEEE Trans. Microw. Theory Tech. **55**, 1209–1218 (2007).
52. M. I. Cheema and A. G. Kirk, "Accurate determination of the quality factor and tunneling distance of axisymmetric resonators for biosensing applications," Opt. Express **21**, 8724–8735 (2013).
53. C.-L. Zou, F.-J. Shu, F.-W. Sun, Z.-J. Gong, Z.-F. Han, and G.-C. Guo, "Theory of free space coupling to high-Q whispering gallery modes," Opt. Express **21**, 9982–9995 (2013).